BULLETIN OF THE POLISH ACADEMY OF SCIENCES
TECHNICAL SCIENCES, Vol. 69(6), 2021, Article number: e139201
DOI: 10.24425/bpasts.2021.139201

SPECIAL SECTION

Transient simulation of a squeeze film damped turbocharger rotor under consideration of fluid inertia and cavitation

Thomas DRAPATOW[1*], **Oliver ALBER**[2], **and Elmar WOSCHKE**[1]

[1] Institute of Mechanics, Otto von Guericke University Magdeburg, 39106 Magdeburg, Germany
[2] MAN Energy Solutions SE, 86153 Augsburg, Germany

Abstract. Squeeze film dampers (SFDs) are commonly used in turbomachinery in order to introduce external damping, thereby reducing rotor vibrations and acoustic emissions. Since SFDs are of similar geometry as hydrodynamic bearings, the REYNOLDS equation of lubrication can be utilised to predict their dynamic behaviour. However, under certain operating conditions, SFDs can experience significant fluid inertia effects, which are neglected in the usual REYNOLDS analysis. An algorithm for the prediction of these effects on the pressure build up inside a finite-length SFD is therefore presented. For this purpose, the REYNOLDS equation is extended with a first-order perturbation in the fluid velocities to account for the local and convective inertia terms of the NAVIER-STOKES equations. Cavitation is taken into account by means of a mass conserving two-phase model. The resulting equation is then discretized using the finite volume method and solved with an LU factorization. The developed algorithm is capable of calculating the pressure field, and thereby the damping force, inside an SFD for arbitrary operating points in a time-efficient manner. It is therefore suited for integration into transient simulations of turbo machinery without the need for bearing force coefficient maps, which are usually restricted to circular centralized orbits. The capabilities of the method are demonstrated on a transient run-up simulation of a turbocharger rotor with two semi-floating bearings. It can be shown that the consideration of fluid inertia effects introduces a significant shift of the pressure field inside the SFDs, and therefore the resulting damper force vector, at high oil temperatures and high rotational speeds. The effect of fluid inertia on the kinematic behaviour of the whole system on the other hand is rather limited for the examined rotor.

Key words: rotor dynamics; journal bearings; squeeze film dampers; fluid inertia.

1. INTRODUCTION

Squeeze film dampers (SFDs) are widely used in turbomachinery to introduce external damping and to reduce rotor vibrations, wear and noise. Due to their simple geometry, their manufacturing costs are relatively low. SFDs can be used in combination with roller bearings or hydrodynamic fluid film bearings. Latter combination is called a semi-floating bearing (see Fig. 1). The SFD consists of a thin lubricant film between a casing and a bushing, whose rotational degree of freedom is locked by appropriate design measures, e.g. axial or radial pins. As can be seen in Fig. 1, the geometric properties of SFDs are quite similar to those of hydrodynamic fluid film bearings. However, as the rotation of the bushing is locked through radial or axial pins, no COUETTE flow can occur inside the lubrication gap. Therefore, only POISSEUILLE flow and squeeze flow are present and the SFD does not show any static stiffness, unless centering springs are installed. A dynamic stiffness can arise due to cross-coupled or anisotropic damping. Although SFDs are simple in geometry, their dynamic properties show strong nonlinearities and are very sensitive to the damper geometry, lubricant viscosity (and therefore lubricant temperature), the current kinematics of the bearing partners and also the current cavitational state inside the lubrication gap. Their behaviour is further influenced by the presence of oil supply grooves and axial seals. The literature regarding SFDs and fluid inertia effects is quite extensive [1–5]. Most literature however is concerned with the determination of force coefficients for circular centered orbits, which is often not sufficient to predict the force response of SFDs for all possible occurring operating conditions in a transient simulation, especially for non centered constructions, since SFDs will often assume highly eccentric elliptical or even chaotic orbits. The goal of this work is therefore to implement a suitable fluid inertia routine into a transient multi-body dynamics simulation without the use of predetermined damper coefficients. The underlying pressure equation will be solved in every time step of the simulation, using accurate and current kinematic quantities and lubricant content of the lubrication gaps, which adds significant computational complexity to the simulation. But the simulation scheme also ensures an accurate prediction of the pressure field and therefore forces response of the simulated SFD at every possible operating point of the SFD. To simulate the pressure distribution inside SFDs, the REYNOLDS equation of lubrication can be solved. However, since the bearing clearance of SFDs is usually quite large, fluid inertia effects can significantly influence their dynamical properties at higher rotational

---

[*] e-mail: thomas.drapatow@ovgu.de

Manuscript submitted 2021-03-31, revised 2021-07-29, initially accepted for publication 2021-08-19, published in December 2021

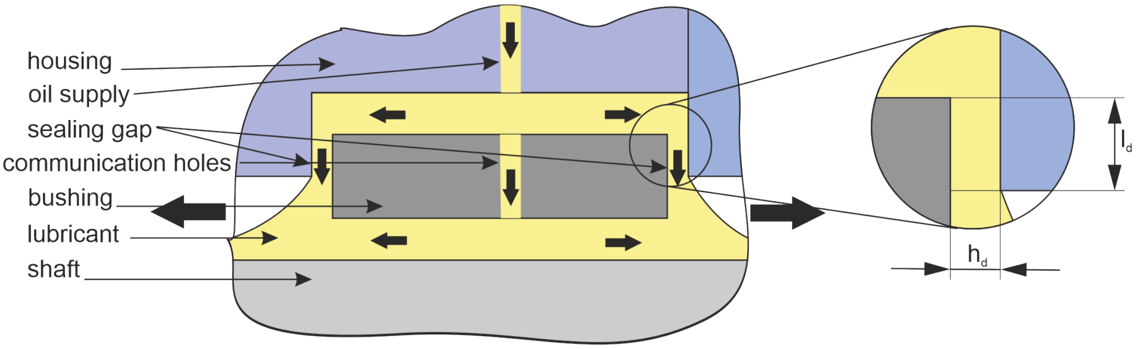

Fig. 1. Structure of a semi-floating-bearing. The upper squeeze film is axially sealed by means of an axial sealing gap

speeds. These effects are neglected in the classical REYNOLDS equation. To estimate the significance of fluid inertia, the modified REYNOLDS number

$$\mathrm{Re}^* = \frac{\rho\,\omega\,c^2}{\eta} \tag{1}$$

can be evaluated, where ρ and η are density and viscosity of the lubricant, ω is the circular excitation frequency and c is the bearing clearance. Fluid inertia can be neglected for $\mathrm{Re}^* < 1$ according to SZERI [6]. The modified REYNOLDS number must not be confused with the REYNOLDS number Re, which is used to determine the influence of turbulence. The highest excitation frequency in a rotordynamic system is usually the rotational frequency of the shaft. If subsynchronous excitations are dominating, ω can drop to much lower values. However, it is usually not known a-priori whether subsynchronous excitations are dominant in the system. It is therefore possible that fluid inertia shows no effect on the rotordynamic performance, even though the value of Re^* suggests the presence of significant fluid inertia effects. To introduce fluid inertia effects into the simulation of SFDs, different approaches have been used in the literature. One possibility is the application of commercial three-dimensional CFD software [7,8]. These software packages solve the complete NAVIER-STOKES equations numerically with suitable iteration schemes. The 3D NAVIER-STOKES equations are made up of four coupled partial differential equations, which require computationally expensive iteration schemes to solve. These are too time-consuming to achieve a reasonable fast time integration. Furthermore, unfavorable geometric proportions of the lubrication gap impede meshing and require very small control volumes to avoid a distorted mesh. A similar approach is the so called “Bulk – Flow – Model” (also called “Method of Averaged Inertia”) [9,10]. This method assumes block-shaped velocity profiles in direction of the lubrication gap height and can therefore reduce the 3D – problem to a 2D one, which cuts computational time significantly. However, the usual time-consuming CFD iteration schemes still need to be applied. The assumption of block-shaped velocity profiles is also controversially discussed in the literature [11]. Multiple authors attempted to include fluid inertia effects in a REYNOLDS-like computational scheme, called the extended REYNOLDS equation [1,2]. These schemes usually compute a pressure distribution p_0 with the regular REYNOLDS equation and use this pressure distribution to compute velocity fields. These can then be inserted explicitly or implicitly into the corresponding inertia terms to calculate an approximation of the inertial pressure field p_1. Because of its high computational efficiency, an extended REYNOLDS equation will be utilised in this work.

2. TWO-PHASE CAVITATION MODEL

Cavitation can influence the dynamic properties of SFDs and hydrodynamic bearings significantly, since the viscosity of a mixture of lubricant and air differs drastically from pure lubricant. Consequently, a multitude of algorithms for the prediction of cavitation can be found in the literature. In this work, the so-called Two Phase Cavitation Model (TPM) was chosen, which was first proposed by PEEKEN [12]. Its main advantage is the calculation of a physical pressure inside the cavitated area, which ensures the existence of higher-order spatial pressure derivatives. These derivatives are necessary for the calculation of fluid inertia effects. The TPM assumes that the supplied lubricant is saturated with air at a reference pressure P_{ref}. When the lubricant is exposed to a pressure lower than the reference pressure, the solubility of the dissolved gas declines according to HENRY’s law and air is forced out of the solution. Cavitation bubbles are formed, which are rapidly dissolved as soon as the lubricant is exposed to rising pressure. The BOYLE-MARIOTTE law is used to also include the gas expansion inside the bubbles at lower pressure. Solution and dissolution processes, as well as the bubble expansion and collapse, are assumed to happen instantaneously, transient bubble dynamic effects are not considered. The detailed derivation can be found in references [12,13], the resulting formula to calculate the lubricant mass fraction from the pressure in each control volume is as follows

$$F = \frac{p}{\left(r_{\mathrm{sup}} + \alpha\right) p_{\mathrm{ref}}\,\vartheta_m + (1-\alpha)p}\,. \tag{2}$$

The reference pressure p_{ref} should be set to the ambient pressure of 101.3 kPa in most cases, since the lubricant will usually settle at ambient pressure for some time before being pumped into the SFD and dissolve air accordingly. The BUNSEN coefficient α defines the solubility of gas in the lubricant and amounts to 0.08 for most common mineral oils. r_{sup} describes the fraction of bubbles in the supplied lubricant while ϑ_m is the relative oil temperature

$$\vartheta_m = \frac{T_{\text{oil}}}{T_0}\,, \tag{3}$$

where T_0 is the ambient temperature in K. Air solubility in oil is generally decreased at higher temperatures, which results in earlier onset of cavitation and a smaller lubricant mass fraction as can be seen in Fig. 2. Equation (2) permits lubricant mass fractions $F > 1$ which are not physically feasible. Therefore, mass fractions larger than one are manually set to be one. To complete the cavitation model, a relation between the lubricant mass fraction F and effective fluid density ρ and viscosity η must be defined. It is assumed, that density and viscosity vary linearly with F according to reference [12]

$$\rho = F\rho_{\text{oil}}\,, \tag{4}$$

$$\eta = F\eta_{\text{oil}}\,. \tag{5}$$

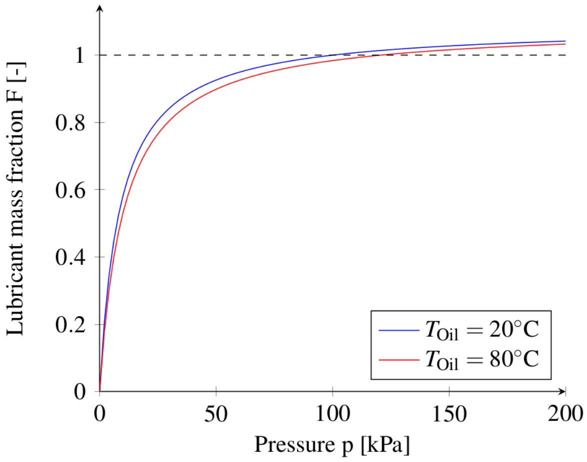

Fig. 2. Relation between lubricant mass fraction F and fluid film pressure p for two different lubricant temperatures

3. FLUID INERTIA CALCULATION SCHEME

The extended RENYOLDS equation is derived from the NAVIER-STOKES equation

$$\rho\underline{\dot{v}} = \rho\left(\frac{\partial\underline{v}}{\partial t} + (\underline{v}\cdot\nabla)\,\underline{v}\right) \tag{6}$$

and the continuity equation

$$\frac{\partial\rho}{\partial t} + \frac{\partial(\rho u)}{\partial x} + \frac{\partial(\rho v)}{\partial y} + \frac{\partial(\rho w)}{\partial z} = 0. \tag{7}$$

The NAVIER-STOKES equation (6) can be simplified by introducing the following assumptions based on the geometry and kinematics of squeeze film dampers:

- The pressure is constant over the gap height z.
- All gradients of the velocity in direction of the gap height z are negligible.
- The velocity gradients of the circumferential velocity u and axial velocity v in circumferential and axial direction x, y are negligible compared to the gradients in z-direction.
- The gap height is small compared to the damper radius and its width.
- The bearing surfaces are smooth and the no-slip-condition is satisfied.
- The bearing partners show small curvature in relation to each other. The lubrication gap can therefore be unrolled and analyzed in cartesian coordinates.

The component wise simplified NAVIER-STOKES equations then result in

$$\rho\left(\frac{\partial u}{\partial t} + u\frac{\partial u}{\partial x} + v\frac{\partial u}{\partial y} + w\frac{\partial u}{\partial z}\right) = -\frac{\partial p_h}{\partial x} + \frac{\partial}{\partial z}\left(\eta\frac{\partial u}{\partial z}\right), \tag{8}$$

$$\rho\left(\underbrace{\frac{\partial v}{\partial t}}_{\text{Local inertia}} + \underbrace{u\frac{\partial v}{\partial x} + v\frac{\partial v}{\partial y} + w\frac{\partial v}{\partial z}}_{\text{Convective inertia}}\right) = -\frac{\partial p_h}{\partial y} + \frac{\partial}{\partial z}\left(\eta\frac{\partial v}{\partial z}\right). \tag{9}$$

On the left-hand side, the fluid inertia components, which are eliminated in the derivation of the regular REYNOLDS equation, are retained. The boundary conditions for the velocity profiles u and v are determined using the no-slip-condition and are as follows

$$\begin{aligned} u(z=0) &= 0,\\ u(z=h) &= 0,\\ v(z=0) &= 0,\\ v(z=h) &= 0. \end{aligned} \tag{10}$$

These boundary conditions differ from those in plain bearings, since the domain boundaries of SFDs are stationary in terms of x. It is assumed, that the velocity profiles in circumferential and width direction u, v are dominated by the pressure and viscous term on the right hand sides of equations (8) and (9). Velocity approximations u_0, v_0 can therefore be derived by setting the left-hand sides of equations (8) and (9) to zero, integrating the right-hand sides twice over z and eliminating the integration constants with the boundary conditions (10)

$$u_0 = \frac{1}{2\eta}\frac{\partial p_0}{\partial x}\left(z^2 - hz\right), \tag{11}$$

$$v_0 = \frac{1}{2\eta}\frac{\partial p_0}{\partial y}\left(z^2 - hz\right). \tag{12}$$

Inserting the inertialess velocity profiles (equationss (11 and 12)) into the continuity equation (cf. equation (7)) and integrating over z, the regular REYNOLDS equation is obtained

$$\frac{\partial}{\partial x}\left(\frac{\rho h^3}{12\eta}\frac{\partial p_0}{\partial x}\right) + \frac{\partial}{\partial y}\left(\frac{\rho h^3}{12\eta}\frac{\partial p_0}{\partial y}\right) = \frac{(\rho h)}{\partial t}, \tag{13}$$

which can be used to explicitly calculate the inertialess pressure approximation p_0. With a known pressure distribution, the now implicitly known inertialess velocity profiles u_0, v_0, w_0 can be substituted into the left-hand side of equations (8) and (9). The fluid velocities u, v and pressure p on the right-hand side are replaced with the inertially corrected unknowns u_1, v_1 and p_1

$$\rho\left(\frac{\partial u_0}{\partial t}+u_0\frac{\partial u_0}{\partial x}+v_0\frac{\partial u_0}{\partial y}+w_0\frac{\partial u_0}{\partial z}\right)=-\frac{\partial p_1}{\partial x}+\frac{\partial}{\partial z}\left(\eta\frac{\partial u_1}{\partial z}\right), \tag{14}$$

$$\rho\left(\frac{\partial v_0}{\partial t}+u_0\frac{\partial v_0}{\partial x}+v_0\frac{\partial v_0}{\partial y}+w_0\frac{\partial v_0}{\partial z}\right)=-\frac{\partial p_1}{\partial y}+\frac{\partial}{\partial z}\left(\eta\frac{\partial v_1}{\partial z}\right). \tag{15}$$

The aforementioned steps that led from equation (8) to equation (13) can now be repeated to derive the extended REYNOLDS equation. By integrating twice over z and solving equations (14) and (15) for u_1, v_1 by taking into account the velocity boundary conditions (10), corrected velocity profiles are obtained as a function of p_0 and p_1

$$\begin{aligned}u_1=&\left(\frac{z^6\rho}{240\eta^3}-\frac{zh^5\rho}{480\eta^3}-\frac{z^5h\rho}{80\eta^3}+\frac{z^4h^2\rho}{96\eta^3}\right)\cdot\frac{\partial}{\partial x}\left[\left(\frac{\partial p_0}{\partial x}\right)^2+\left(\frac{\partial p_0}{\partial y}\right)^2\right]\\&+\left(\frac{zh^5\rho}{240\eta^4}-\frac{z^6\rho}{120\eta^4}+\frac{z^5h\rho}{40\eta^4}-\frac{z^4h^2\rho}{48\eta^4}\right)\cdot\frac{\partial p_0}{\partial x}\left(\frac{\partial p_0}{\partial x}\frac{\partial\eta}{\partial x}+\frac{\partial p_0}{\partial y}\frac{\partial\eta}{\partial y}\right)\\&+\left(\frac{z^4h\rho}{48\eta^3}-\frac{zh^4\rho}{120\eta^3}-\frac{z^5\rho}{80\eta^3}\right)\frac{\partial p_0}{\partial x}\left(\frac{\partial p_0}{\partial x}\frac{\partial h}{\partial x}+\frac{\partial p_0}{\partial y}\frac{\partial h}{\partial y}\right)\\&+\left(\frac{z^4\rho}{24\eta^2}+\frac{zh^3\rho}{24\eta^2}-\frac{z^3h\rho}{12\eta^2}\right)\frac{\partial^2p_0}{\partial x\partial t}\\&+\left(\frac{z^3h\rho}{12\eta^3}-\frac{zh^3\rho}{24\eta^3}-\frac{z^4\rho}{24\eta^3}\right)\frac{\partial p_0}{\partial x}\frac{\partial\eta}{\partial t}\\&+\left(\frac{zh^2\rho}{12\eta^2}-\frac{z^3\rho}{6\eta^2}+\frac{z^4\rho}{12\eta^2h}\right)\frac{\partial p_0}{\partial x}\frac{\partial h}{\partial t}\\&+\left(\frac{z^2}{2\eta}-\frac{zh}{2\eta}\right)\frac{\partial p_1}{\partial x},\end{aligned}\tag{16}$$

a similar formulation for v_1 can be found by swapping the derivatives after x and y in equation (16). These corrected velocity profiles are then substituted into the continuity equation (cf. equation (7)) and integrated over z. Introducing suitable nondimensional quantities

$$\begin{aligned}H&=\frac{h}{\Delta r_I}, & X&=\frac{x}{r_I}, & Y&=\frac{Y}{r_I},\\P&=\frac{p\,c^2}{r_I\,\eta^*\,u^*}, & \mathrm{Re}^*&=\frac{\rho\,c^2\,\omega}{\eta}, & T&=\frac{t\,u^*}{r_I}\end{aligned}\tag{17}$$

yields an extended REYNOLDS equation, including a fluid inertia correction

$$\begin{aligned}0=&-\frac{\partial}{\partial X}\left(\frac{H^3}{12}\frac{\partial P_1}{\partial X}\right)-\frac{\partial}{\partial Y}\left(\frac{H^3}{12}\frac{\partial P_1}{\partial Y}\right)+\frac{\partial(FH)}{\partial T}\\&+\mathrm{Re}^*\frac{\partial}{\partial X}\left\{\frac{H^7}{1120F^2}\frac{\partial P_0}{\partial X}\left(\frac{\partial F}{\partial X}\frac{\partial P_0}{\partial X}+\frac{\partial F}{\partial Y}\frac{\partial P_0}{\partial Y}\right)\right.\\&-\frac{H^7}{1120F}\frac{\partial}{\partial X}\left[\left(\frac{\partial P_0}{\partial X}\right)^2+\left(\frac{\partial P_0}{\partial Y}\right)^2\right]\\&-\frac{H^6}{480F}\frac{\partial P_0}{\partial X}\left[\frac{\partial H}{\partial X}\frac{\partial P_0}{\partial X}+\frac{\partial H}{\partial Y}\frac{\partial P_0}{\partial Y}\right]+\frac{H^5}{120}\frac{\partial^2P_0}{\partial X\partial T}\\&\left.-\frac{H^5}{120F}\frac{\partial F}{\partial T}\frac{\partial P_0}{\partial X}+\frac{H^4}{60}\frac{\partial P_0}{\partial X}\frac{\partial H}{\partial T}\right\}\\&+\mathrm{Re}^*\frac{\partial}{\partial Y}\left\{\frac{H^7}{1120F^2}\frac{\partial P_0}{\partial Y}\left(\frac{\partial F}{\partial Y}\frac{\partial P_0}{\partial Y}+\frac{\partial F}{\partial X}\frac{\partial P_0}{\partial X}\right)\right.\\&-\frac{H^7}{1120F}\frac{\partial}{\partial Y}\left[\left(\frac{\partial P_0}{\partial Y}\right)^2+\left(\frac{\partial P_0}{\partial X}\right)^2\right]\\&-\frac{H^6}{480F}\frac{\partial P_0}{\partial Y}\left[\frac{\partial H}{\partial Y}\frac{\partial P_0}{\partial Y}+\frac{\partial H}{\partial X}\frac{\partial P_0}{\partial X}\right]+\frac{H^5}{120}\frac{\partial^2P_0}{\partial Y\partial T}\\&\left.-\frac{H^5}{120F}\frac{\partial F}{\partial T}\frac{\partial P_0}{\partial Y}+\frac{H^4}{60}\frac{\partial P_0}{\partial Y}\frac{\partial H}{\partial T}\right\}.\end{aligned}\tag{18}$$

By isolating the first two summands with the unknowns P_1 on the left-hand side, it can immediately be seen that the left-hand sides of the REYNOLDS equation (13) and the extended REYNOLDS equation (18) are indeed identical. This circumstance can be used later to accelerate the numerical solution of the extended REYNOLDS equation by saving and reusing the factorized system matrix. The right-hand side of equation (18) contains only known values, the derivatives of pressure and lubricant mass fraction can be calculated with finite difference schemes. The nondimensionalization is carried out to improve the condition of the resulting system matrix, it also reveals the linear dependence of the inertial correction on the extended REYNOLDS number Re^*. The calculated pressure field P_1 can then be integrated over the solution domain to obtain the forces and moments exerted by the SFD.

4. SOLUTION STRATEGY

4.1. Time integration

The goal is the simulation of a transient run-up of a rotor with a semi-floating bearing configuration. It is therefore not sufficient to only calculate the forces of the SFD, but a whole multi body simulation including the elasticity of the rotor, gyroscopic effects and kinematics of the SFD bushings is necessary. The developed algorithm was therefore implemented into the multi body dynamics software EMD. The general calculation scheme is depicted in Fig. 3. The differential kinematics equation

$$\underline{\underline{M}}(\underline{y})\cdot\underline{\ddot{y}}+\underline{h}_{\omega}(\underline{\dot{y}})+\underline{h}_{el}(\underline{y},\underline{\dot{y}})=\underline{h}_{e}(t,\underline{y},\underline{\dot{y}}) \tag{19}$$

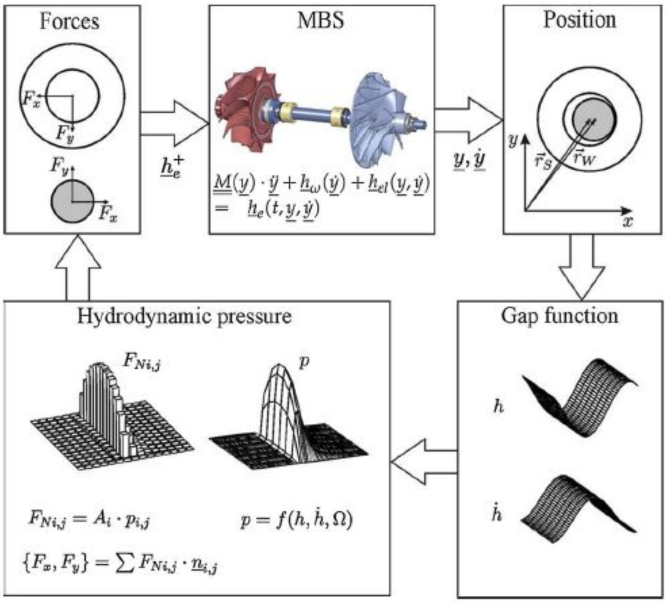

Fig. 3. General workflow of time integration in EMD [14]

is solved for the state vector $\underline{y}$ with a suitable time integration scheme. $\underline{\underline{M}}$ is defined as the mass matrix of the whole system while $\underline{h}_\omega$, $\underline{h}_{el}$, $\underline{h}_e$ contain the gyroscopic forces, elastic forces and external forces respectively. After each update of the state vector, the new positions and velocities of the bearing partners can be used to obtain an updated fluid film gap function h and its temporal derivative $\frac{\partial h}{\partial t}$, which in turn are used as input for the hydrodynamics routine to calculate fluid film pressures and fluid film reaction forces. These forces are then fed back as external forces in $\underline{h}_e$ for the next time step of the multi-body dynamics routine. Depending on the properties of the system and the simulated time frame, the whole integration procedure can take millions of time steps. By far the most expensive task in terms of calculations is the repeated solution of the REYNOLDS equation inside the hydrodynamics routine. It is therefore of utmost importance to keep the hydrodynamics solution as time efficient as possible.

4.2. Solution of the REYNOLDS equation

The preferred numerical method for most fluid dynamics computations is the finite volume method since its balancing of fluid flow over the control volumes inherently guarantees mass conservation [15]. The fluid films are unwrapped and discretized with equidistant rectangular finite volumes. The REYNOLDS equation is then numerically integrated over all finite volumes. The discretization for the POISSEUILLE and squeeze term can be taken from the literature [14] as is demonstrated on the POISSEUILLE term in circumferential direction

$$\int_0^{\Delta X}\int_0^{\Delta Y}\left(\frac{H^3}{12}\frac{\partial P_0}{\partial X}\right)\mathrm{d}X\,\mathrm{d}Y = \left(\frac{H^3}{12}\frac{\partial P_0}{\partial X}\right)^e \Delta Y - \left(\frac{H^3}{12}\frac{\partial P_0}{\partial X}\right)^w \Delta Y, \tag{20}$$

where the lower case indices e and w denote the control volume borders as depicted in Fig. 4. Since dimensionless pressure P_0 and fluid gap height H are only known at the nodes denoted with capital letters in Fig. 4, they need to be linearly interpolated and derivatives are formulated using a central finite difference scheme

$$H^e = \frac{H^C + H^E}{2}, \tag{21}$$

$$\frac{\partial P_0^{e,w}}{\partial X} = \frac{P_0^{E,C} - P_0^{C,W}}{\Delta X}. \tag{22}$$

The procedure is repeated for the extended REYNOLDS equation (18) which is again demonstrated using the circumferential term, where the term inside the curly bracket is abbreviated with I_x

$$\int_0^{\Delta X}\int_0^{\Delta Y} \mathrm{Re}^* \frac{\partial}{\partial X}\{I_x\}\,\mathrm{d}X\,\mathrm{d}Y = (I_x^e - I_x^w)\,\Delta Y. \tag{23}$$

Since I_x contains higher-order derivatives and mixed derivatives of P_0, some more elaborate finite difference schemes are necessary

$$\frac{\partial^2 P_0^e}{\partial X^2} = \frac{P_0^{EE} - 2P_0^C + P_W}{2\Delta X^2}, \tag{24}$$

$$\frac{\partial^2 P_0^e}{\partial X \partial Y} = \frac{P_0^{NE} - P_0^{SE} - P_0^N + P_0^S}{2\Delta X \Delta Y}. \tag{25}$$

For temporal derivatives, backwards differences with pressure values from the last time step are used. In the areas of oil supply grooves, the pressure is set to the oil supply pressure while at the axial boundaries of the inner film, the pressure is set to the ambient pressure p_{amb}. To simulate the sealing effect of the axial gap, a volumetric flow balance for the gap is formulated as a boundary condition

$$\frac{\partial p}{\partial x} = \frac{h_d^3}{h^3}\frac{p_{\mathrm{amb}} - p}{l_d}, \tag{26}$$

where h_d and l_d are the height and length of the axial gap.

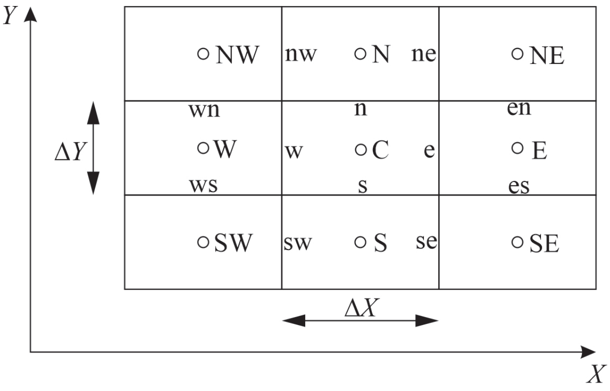

Fig. 4. Indexing of control volumes in the lubrication gap

5. VALIDATION AGAINST EXPERIMENTAL TURBOCHARGER RUN-UP

The simulation algorithm was validated against an experimental turbocharger run-up. The experimental data was provided by MAN Energy Solutions SE. The rotor has two radial hydrodynamic bearings fitted with non-centralized SFDs, both SFDs are axially sealed by means of an axial sealing gap and are supplied via circumferential feeding grooves. Multiple communication bores inside the groove supply the inner lubrication films with oil. For confidentiality reasons, detailed rotor measurements are not provided. All experimental and simulation data is given in dimensionless quantities. Rotor vibrations were measured in two planes adjacent to the compressor and turbine side bearing, marked with CS and TS in Fig. 5. Temperatures were also measured inside the floating rings, which made temperature assumptions – and therefore viscosity assumptions – for both fluid films possible. The SFDs show modified REYNOLDS numbers $\mathrm{Re}^* \approx 2$ at their maximum rotational speed, which according to literature should have a noticeable effect on the SFDs performance. Overall, three simulations with varying model complexity were carried out to determine the calculational cost and added value of the TPM and the fluid inertia model. The rotor vibrations next to the turbine side bearings were then rendered as spectrograms by means of the Superlet Transformation [16], which improves time and frequency resolution compared to the often used FOURIER transformation and does not produce amplitude errors, even for highly transient signals. At first, a simple calculation with the GÜMBEL (or half-SOMMERFELD) cavitation model was carried out, where subatmospheric pressures are simply set to the atmospheric pressure and no pressure iteration occurs. The comparison with the experimental result can be seen in Fig. 6 and is summarized in Table 1. Simulation and experiment are in good agreement. Two subsynchronous excitations – a distinct one and a rather weakly pronounced one – were predicted correctly in starting frequency and amplitude. However, their amplitudes subside rather quickly in the simulation but stay persistent in the experiment. The synchronous excitation was underpredicted by a factor of 0.5. With the addition of the TPM (Fig. 7) the persistence of the subsynchronous excitation was predicted correctly. However, its amplitude was now too high by a factor of 1.7, since the TPM lowers the fluid content and therefore the damping capacity of the simulated fluid films. The synchronous amplitude is raised marginally, but is still underpredicted. Underprediction of synchronous excitation and simultaneous overprediction of subsynchronous excitation can be caused by faulty load assumptions. If the unbalance is significantly higher than anticipated or if turbine and compressor unbalance are out of phase, the synchronous amplitude is

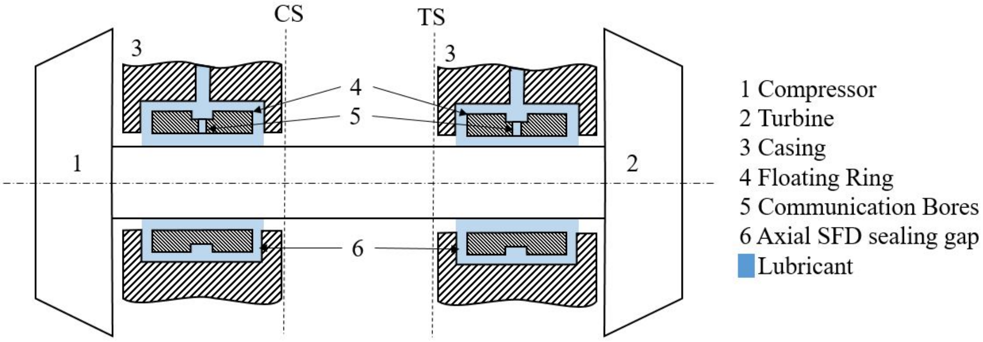

Fig. 5. Topology of a turbocharger rotor with two semi-floating bearings and axially sealed SFDs

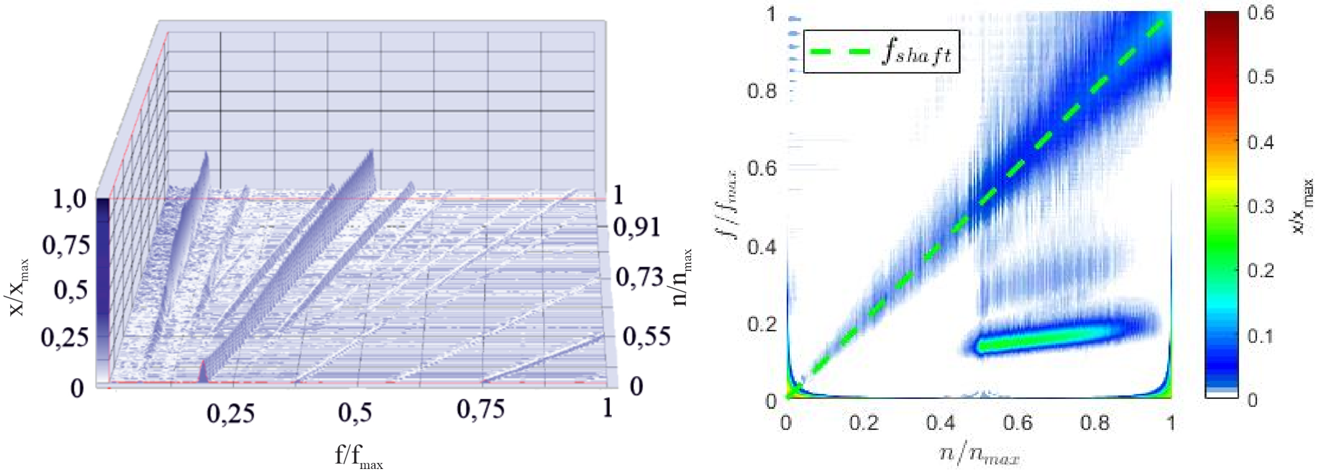

Fig. 6. Spectrogram of the shaft vibrations in the TS plane. Left: experimental results, Right: simulation result with GÜMBEL cavitation model. Note that the axes are flipped

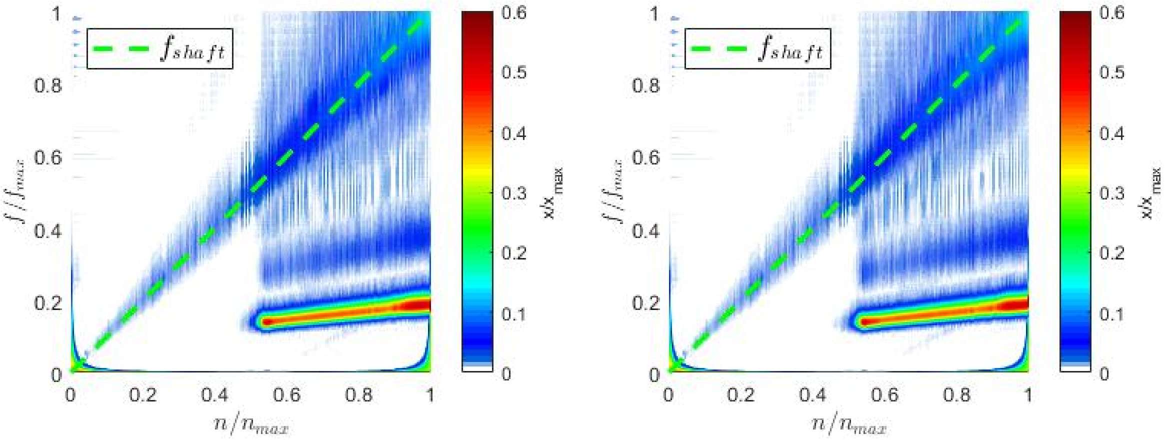

Fig. 7. Spectrogram of the shaft vibrations in the TS plane. Left: simulation result with TPM and no fluid inertia effects. Right: simulation result with the TPM and fluid inertia effects

Table 1

Dimensionless comparison of different simulation models with the experiment

Criteria	Experiment	GÜMBEL cavitation, no inertia	TPM, no inertia	TPM and inertia
Sub 1 starting frequency	0.5	0.5	0.5	0.5
Sub 1 subsiding frequency	> 1	0.91	> 1	> 1
Sub 1 max. amplitude	0.3	0.3	0.52	0.52
Synchronous excitation max. amplitude	0.25	0.12	0.14	0.14
Simulation duration [h:min]	–	2:08	15:44	18:42

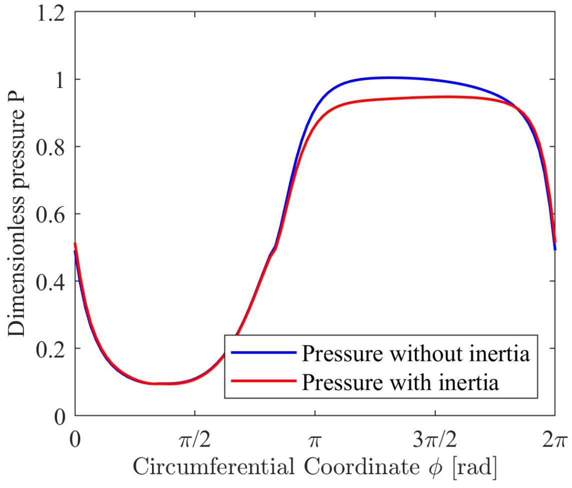

Fig. 8. Dimensionless circumferential pressure distribution of the compressor side SFD in a bearing land midplane

raised. Rising synchronous excitation in turn can suppress subsynchronous oscillations. It should also be noted that the calculation model did not include an axial bearing which can also influence radial rotor vibrations significantly.

The inclusion of fluid inertia effects did not influence the rotor performance at all, as can be seen in Fig. 7. This result seems to contradict literature sources that predict fluid inertia effects at $\mathrm{Re}^* > 1$ [17, 18]. Most works however assume centered circular orbits for their predictions, which holds true for SFDs with centralizing springs. However, in the calculated example, the SFDs operate with very high eccentricity. The turbine side SFD for example stays in contact with the housing over the whole simulation duration while the compressor side SFD operates at relative eccentricities $\varepsilon > 0.6$. The influence of fluid inertia on the pressure distribution of the compressor side SFD at maximum rotational speed is depicted in Fig. 8. A direct comparison between the pressure build ups of different simulations was not possible, since the SFDs will assume slightly different orbits in the presence of fluid inertia. Instead, the pressure distribution with and without fluid inertia were defined as output, while the bearing forces were calculated with the inertial pressure distribution. It can be seen, that the influence on pressure distribution is noticeable. It results in a reduction of the resulting SFD force of about 4.2 % and a phase shift of the force vector of 2 degrees. Since the SFD does not operate in a circular centered orbit, those values are not constant for the whole orbit. A distinctive shift of the pressure field compared to the inertialess solution as it can be found in literature (e.g. [2]) is not present. The reason for this difference lies within the different operating conditions. The orbit of the squeeze film damper is neither circular nor centralized and the lubricant is cavitated. If a circular, centralized orbit is assumed, the model can accurately reproduce the pressure shift from literature.

6. CONCLUSION

An algorithm for transient simulations of squeeze film damped rotors, including inertia effects and cavitation, was presented and validated with experimental results. The algorithm is capable to deliver results within a reasonable time frame. Good agreement with an experimental result was achieved. The fluid inertia did influence the calculated pressure fields, but had little to no effect on the dynamic behaviour of the whole rotor, despite the relatively high modified REYNOLDS number $\mathrm{Re}^* = 2$ of the installed SFDs. The result suggests, that the rotordynamics of the examind turbocharger are dominated by different effects, like contact between the floating bushings and the housing and by the properties of the inner fluid films, which do not show significant inertia effects. It may therefore be possible to neglect fluid inertia even for $\mathrm{Re}^* > 1$ in semi-floating bearings in order to reduce the model complexity and calculation time. Further investigations should focus on the influence of turbulence and the pressure field in deep oil supply grooves of SFDs.

ACKNOWLEDGEMENTS

The research project (FVV project no. 1291) was performed by the Junior Professorship Fluid Structure Interaction in Multibody Systems (FSK) at the Institute of Mechanics of the Otto von Guericke University Magdeburg under the direction of Jun.-Prof. Dr.-Ing. Elmar Woschke. Based on a decision taken by the German Bundestag, it was supported by the Federal Ministry for Economic Affairs and Energy (BMWi) and the AIF (German Federation of Industrial Research Associations eV) within the framework of the industrial collective research (IGF) programme (IGF no. 19669 BR). The project was conducted by an expert group led by Dipl.-Ing. Thomas Klimpel (ABB Schweiz AG, Turbocharging ltd). The authors gratefully acknowledge the support received from the funding organisations, from the FVV (Research Association for Combustion Engines eV) and from all those involved in the project.

REFERENCES

[1] M.B. Banerjee, R. Shandil, S. Katyal, G. Dube, T. Pal, and K. Banerjee, “A nonlinear theory of hydrodynamic lubrication,” *J. Math. Anal. Appl.*, vol. 117, no. 1, pp. 48–56, 1986.

[2] S. Hamzehlouia and K. Behdinan, “Squeeze film dampers supporting high-speed rotors: Fluid inertia effects,” *Proc. Inst. Mech. Eng., Part J: J. Eng. Tribol.*, vol. 234, no. 1, pp. 18–32, 2020.

[3] M. Ramli, J. Ellis, and J. Roberts, “On the computation of inertial coefficients in squeeze-film bearings,” *Proc. Inst. Mech. Eng., Part C: J. Mech. Eng. Sci.*, vol. 201, no. 2, pp. 125–131, 1987, doi: 10.1243/PIME_PROC_1987_201_095_02.

[4] E. Reinhardt and J. Lund, “Influence of fluid inertia on the dynamic properties of journal bearings.” *J. Lubr. Technol.*, vol. 97 Ser F, no. 2, pp. 159–167, 1975.

[5] A.Z. Szeri, A.A. Raimondi, and A. Giron-Duarte, “Linear Force Coefficients for Squeeze-Film Dampers,” *J. Lubr. Technol.*, vol. 105, no. 3, pp. 326–334, 07 1983.

[6] A.Z. Szeri, *Fluid Film Lubrication: Theory and Design*. Cambridge University Press, 1998.

[7] Z. Guo, T. Hirano, and R.G. Kirk, “Application of CFD analysis for rotating machinery: Part 1 — hydrodynamic, hydrostatic bearings and squeeze film damper,” in *Volume 4: Turbo Expo 2003*. ASME, 2003, doi: 10.1115/gt2003-38931.

[8] C. Xing, M.J. Braun, and H. Li, “A three-dimensional navier-stokes- based numerical model for squeeze film dampers. part 2—effects of gaseous cavitation on the behavior of the squeeze film damper,” *Tribol. Trans.*, vol. 52, no. 5, pp. 695–705, Sep 2009, doi: 10.1080/10402000902913311.

[9] V. Constantinescu, *Laminar Viscous Flow*. Berlin Heidelberg: Springer Science & Business Media, 2012.

[10] J. Gehannin, M. Arghir, and O. Bonneau, “Complete squeezefilm damper analysis based on the “bulk flow” equations,” *Tribol. Trans.*, vol. 53, no. 1, pp. 84–96, 2009, doi: 10.1080/10402000903226382.

[11] S. Lang and S. Verlag, *Effiziente Berechnung von Gleitlagern und Dichtspalten in Turbomaschinen*, ser. Forschungsberichte zur Fluidsystemtechnik. Shaker Verlag, 2018.

[12] H. Peeken and J. Benner, “Beeinträchtigung des Druckaufbaus in *Gleitlagern durch Schmierstoffverschäumung,” in Gleit- und Wälzlagerungen: Gestaltung, Berechnung, Einsatz; Tagung Neu-Ulm, 14. und 15. März 1985 / VDI-Ges. Entwicklung, Konstruktion, Vertrieb. – (VDI-Berichte; 549)*, 2013, pp. 373–397.

[13] Ü. Mermertas, “Nichtlinearer Einfluss von Radialgleitlagern auf die Dynamik schnelllaufender Rotoren, Dissertation,” Düren, Aachen, 2003.

[14] E. Woschke, C. Daniel, and S. Nitzschke, “Excitation mechanisms of non-linear rotor systems with floating ring bearings – simulation and validation,” *Int. J. Mech. Sci.*, vol. 134, pp. 15–27, 2017, doi: 10.1016/j.ijmecsci.2017.09.038.

[15] R. Eymard, G. Thierry, and R. Herbin, “Handbook of numerical analysis,” vol. 7, pp. 731–1018, 01 2000.

[16] V.V. Moca, A. Nagy-Dăbâcan, H. Bârzan, and R. C. Mure¸san, “Superlets: time-frequency super-resolution using wavelet sets,” *bioRxiv*, 2019.

[17] S. Hamzehlouia and K. Behdinan, “A study of lubricant inertia effects for squeeze film dampers incorporated into highspeed turbomachinery,” *Lubricants*, vol. 5, p. 43, 10 2017, doi: 10.3390/lubricants5040043.

[18] L. San Andrés and J. Vance, “Effects of fluid inertia and turbulence on the force coefficients for squeeze film dampers,” *J. Eng. Gas Turbines Power*, vol. 108, 04 1986, doi: 10.1115/1.3239908.